

# Acetylene Black Induced Heterogeneous Growth of Macroporous CoV<sub>2</sub>O<sub>6</sub> Nanosheet for High-Rate Pseudocapacitive Lithium-Ion Battery Anode

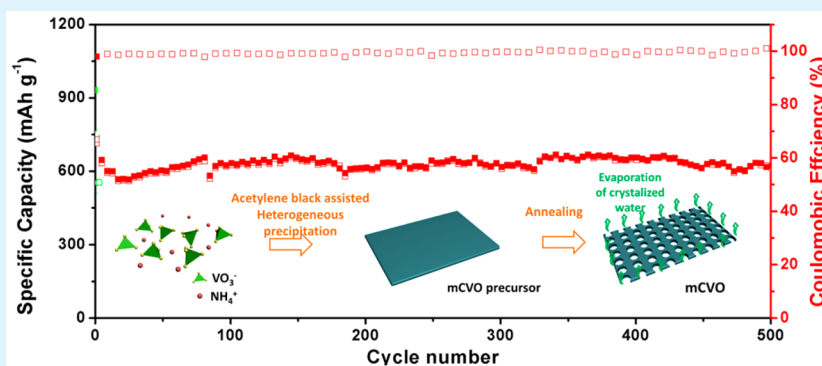
Lei Zhang,<sup>†</sup> Kangning Zhao,<sup>†</sup> Yanzhu Luo,<sup>†</sup> Yifan Dong,<sup>†,‡</sup> Wangwang Xu,<sup>§</sup> Mengyu Yan,<sup>†</sup> Wenhao Ren,<sup>†</sup> Liang Zhou,<sup>\*,†</sup> Longbing Qu,<sup>†</sup> and Liqiang Mai<sup>\*,†</sup>

<sup>†</sup>State Key Laboratory of Advanced Technology for Materials Synthesis and Processing, Wuhan University of Technology, Hubei, Wuhan 430070, China

<sup>‡</sup>Department of Chemistry, University of Wisconsin—Madison, 1101 University Avenue, Madison, Wisconsin 53706, United States

<sup>§</sup>Department of Mechanical and Industrial Engineering, Louisiana State University, Baton Rouge, Louisiana 70830, United States

## Supporting Information



**ABSTRACT:** Metal vanadates suffer from fast capacity fading in lithium-ion batteries especially at a high rate. Pseudocapacitance, which is associated with surface or near-surface redox reactions, can provide fast charge/discharge capacity free from diffusion-controlled intercalation processes and is able to address the above issue. In this work, we report the synthesis of macroporous CoV<sub>2</sub>O<sub>6</sub> nanosheets through a facile one-pot method via acetylene black induced heterogeneous growth. When applied as lithium-ion battery anode, the macroporous CoV<sub>2</sub>O<sub>6</sub> nanosheets show typical features of pseudocapacitive behavior: (1) currents that are mostly linearly dependent on sweep rate and (2) redox peaks whose potentials do not shift significantly with sweep rate. The macroporous CoV<sub>2</sub>O<sub>6</sub> nanosheets display a high reversible capacity of 702 mAh g<sup>-1</sup> at 200 mA g<sup>-1</sup>, excellent cyclability with a capacity retention of 89% (against the second cycle) after 500 cycles at 500 mA g<sup>-1</sup>, and high rate capability of 453 mAh g<sup>-1</sup> at 5000 mA g<sup>-1</sup>. We believe that the introduction of pseudocapacitive properties in lithium battery is a promising direction for developing electrode materials with high-rate capability.

**KEYWORDS:** heterogeneous growth, macroporous nanosheet, CoV<sub>2</sub>O<sub>6</sub>, pseudocapacitance, lithium-ion battery

## INTRODUCTION

With the increasing market of hybrid electric vehicles, electric vehicles, as well as large-scale energy storage systems, lithium-ion batteries (LIBs) and supercapacitors (SCs) have attracted increasingly active research and discussion.<sup>1–8</sup> However, their performance still lags behind the increasing demands of emerging applications. The urgent demand for energy storage worldwide stimulates the researchers to develop electrodes with both high energy and power densities.<sup>9–12</sup> Therefore, it is of great significance for researchers to find new materials or engineer the old materials better for storing and delivering large amounts of energy with sufficient rate capability. Pseudocapacitance arises when reversible redox reactions occur at or near the surface of an active material in contact with an electrolyte, or when these reactions are not limited by solid-state ion

diffusion.<sup>13–16</sup> In this way, high-rate capability can be achieved through fast capacitive reactions for energy storage device. Thus, it is promising when enhanced pseudocapacitance is utilized in electrode materials for high-rate LIBs.

Recently, mixed transition metal oxides are regarded as promising candidates for applications in many fields such as catalysis<sup>17</sup> as well as electrodes for SCs and LIBs,<sup>18,19</sup> because of their complex chemical composition, interfacial effects, and the synergic effects of the multiple metal species.<sup>18,19</sup> As an important family of transition metal oxides, metal vanadates, despite the first research on their electrochemical properties in

Received: January 17, 2016

Accepted: March 3, 2016

Published: March 3, 2016

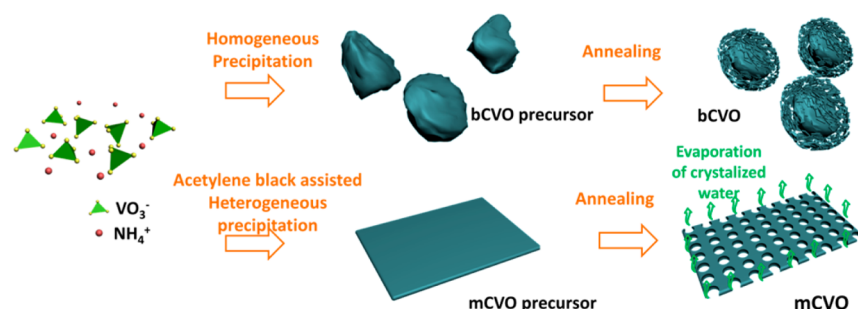


**Figure 1.** Schematic illustration of the formation process of mCVO and bCVO.

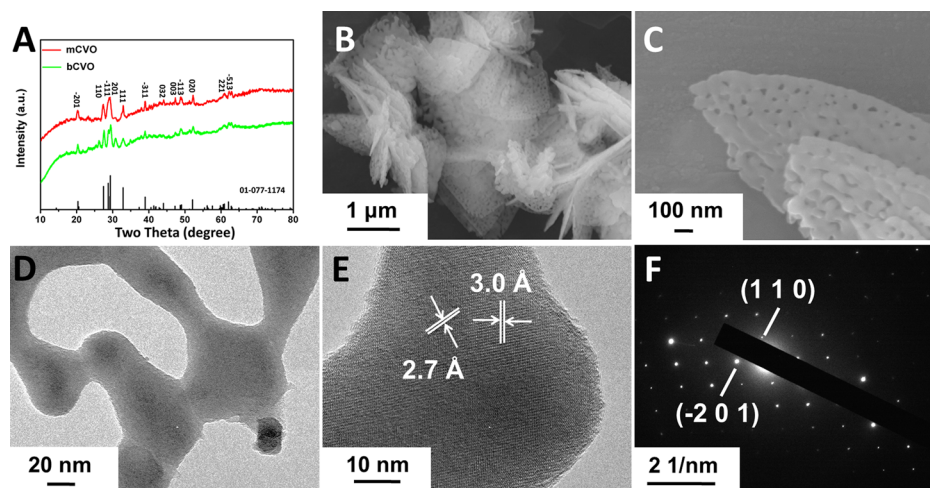


**Figure 2.** (A) XRD patterns of mCVO and bCVO. (B, C) SEM images of mCVO. (D, E) TEM images of mCVO. (F) The corresponding SAED pattern of mCVO.

1999 by Denis et al.,<sup>20</sup> still remain largely unexplored.<sup>21–29</sup> Recently, Wang and his co-workers reported the synthesis of  $\text{Co}_3\text{V}_2\text{O}_8$  multilayered nanosheets as a promising anode for lithium-ion batteries. The reaction mechanism of  $\text{Co}_3\text{V}_2\text{O}_8$  is also investigated where reversible conversion reactions between  $\text{CoO}$  and  $\text{Co}$  proceed on the amorphous  $\text{Li}_x\text{V}_2\text{O}_5$  matrices.<sup>28</sup> However, metal vanadates often suffer from fast capacity fading especially at a high rate, which results from the large volume deformation, sluggish lithium diffusion, as well as relatively low electronic conductivity.<sup>23,25,28</sup> Hence, the rational construction for a uniform metal vanadate nanostructure to improve electronic and ionic conductivity is highly required, but still remains a serious challenge.<sup>25</sup> In addition, little information was reported on metal vanadate regarding the influence of the morphology on charge storage kinetics.

Herein, we report a facile acetylene black (AB) induced heterogeneous growth of macroporous  $\text{CoV}_2\text{O}_6$  nanosheets (denoted as mCVO). It is demonstrated that AB is able to act as foreign nuclei for heterogeneous growth of uniform nanosheet morphology and the macroporous nanosheet structure is formed after thermal release of the crystallization water. The stable macroporous structure can effectively restrain the large volume expansion/contraction and offer continuous electron pathways, facilitating structural integrity as well as electron transport and shortening lithium diffusion length.<sup>30</sup> The mCVO shows greatly enhanced capacitive contribution and a relative lack of diffusion-controlled process, resulting in significant improvements in the cycling stability as well as rate capability as anode for LIBs.

## EXPERIMENTAL SECTION

**Materials Synthesis. Preparation of the Macroporous  $\text{CoV}_2\text{O}_6$  Nanosheets.** In a typical synthesis, 8 mmol of  $\text{NH}_4\text{VO}_3$  and 80 mg of AB are in turn added in 20 mL deionized water at 80 °C under vigorous stirring. After 2 h stirring to ensure the dissolution of  $\text{NH}_4\text{VO}_3$  and the dispersion of AB in water, 20 mL of 0.2 M cobalt acetate is added dropwise and stirred for 5 h to realize complete precipitation. The precipitate is washed with water and alcohol three times and then dried in vacuum for 8 h. To obtain the macroporous  $\text{CoV}_2\text{O}_6$  nanosheet, the precipitation is then annealed at 450 °C in air for 10 h at a heating rate of 10 °C  $\text{min}^{-1}$ . The bulk CVO (denoted as bCVO) is obtained by the same method only without addition of AB.

**Material Characterization.** X-ray diffraction (XRD) patterns were collected with a D8 Discover X-ray diffractometer with area detector, using  $\text{Cu K}\alpha$  radiation ( $\lambda = 1.5418 \text{ \AA}$ ). The microstructures were observed by field-emission scanning electron microscopy (FESEM) (JEOL-7100F), transmission electron microscopy, and high-resolution transmission electron microscopy (HRTEM) (JEM-2100F). Brunauer–Emmet–Teller (BET) surface area was measured by using Tristar II 3020 instrument. Thermogravimetry (TG) was carried out on a STA449c/3/G (NETZSCH).

**Electrochemical Characterization.** The electrochemical properties were characterized by assembly of CR2016-type coin cells in a glovebox filled with pure argon gas. Lithium metal foils were used as the anode. The cathode electrodes were composed of 70% active material, 20% AB, and 10% sodium alginate binder. The slurry was cast onto Cu foil and dried in a vacuum oven at 150 °C for 2 h. A solution (1 M) of  $\text{LiPF}_6$  in EC/DMC (1:1 vol/vol) was used as the electrolyte. The cells were aged for 12 h before the charge/discharge process to ensure full infiltration of the electrolyte into the electrodes. The mass loading of each electrode is 1.4–2.1  $\text{mg cm}^{-2}$ . Galvanostatic charge/discharge measurement was performed by a multichannel battery testing system (LAND CT2001A), and cyclic voltammetry (0.01–2.5

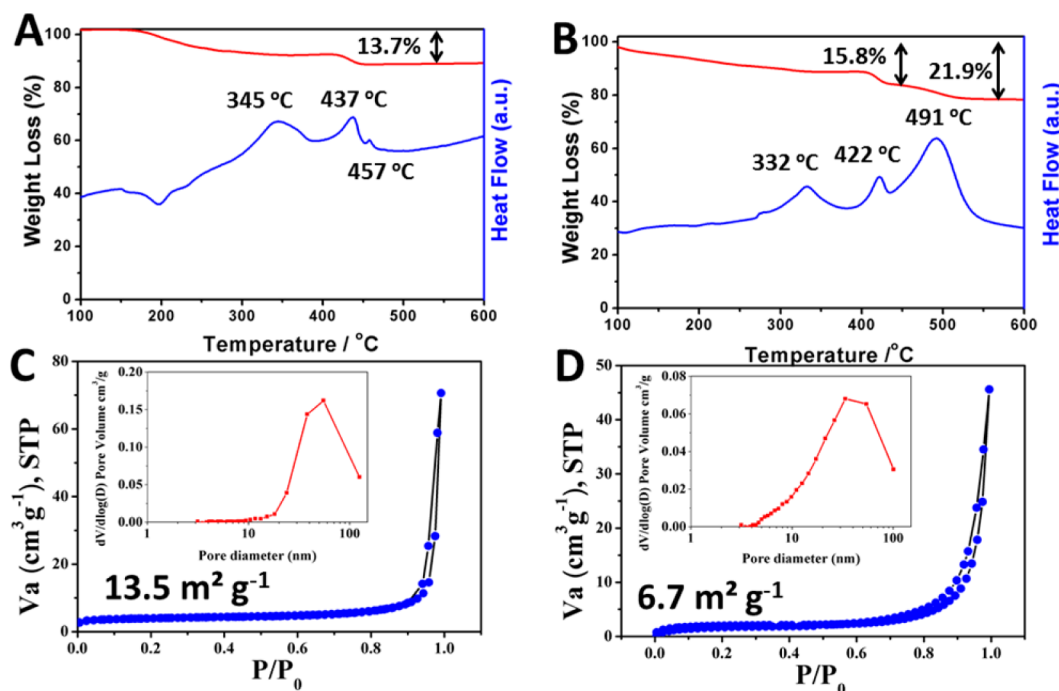


**Figure 3.** (A, B) TG curves and corresponding DSC curves of bCVO and mCVO precursors. (C, D) N<sub>2</sub> adsorption and desorption isotherms of mCVO and bCVO. Insets are the corresponding pore size distributions.

V) was performed using an electrochemical workstation (CHI 760S); electrochemical impedance spectroscopy (EIS) was tested with an Autolab Potentiostat Galvanostat (PGSTAT302N). All the measurements were carried out at room temperature.

## RESULTS AND DISCUSSION

A schematic illustration of AB-assisted heterogeneous formation of mCVO is shown in Figure 1. The first step involves the dissolution of NH<sub>4</sub>VO<sub>3</sub> in water bath process. The introduction of Co<sup>2+</sup> leads to the coprecipitation (Co<sup>2+</sup> + 2VO<sub>3</sub><sup>-</sup> + nH<sub>2</sub>O = CoV<sub>2</sub>O<sub>6</sub>·nH<sub>2</sub>O). In our strategy, AB acts as the foreign active sites for heterogeneous nucleation which occurs at solid–solid interfaces and is thus energetically more favorable. In this way, a smaller critical size and lower formation energy barrier of nuclei are achieved according to the equations for the total Gibbs free energy change ( $\Delta G$ ) below.<sup>31</sup> For homogeneous nucleation, the Gibbs free energy is expressed as  $\Delta G = -a^2h\Delta G_V + 4ah\gamma_s$ , while for heterogeneous nucleation, the Gibbs free energy is expressed as  $\Delta G = -a^2h\Delta G_V + 4ah\gamma_s - ah\gamma_{GB}$  in which  $\Delta G_V$  is the volumetric free energy variation, and  $\gamma_s$  the surface energy increment when a small cuboid-shaped pit having  $a$  in width and  $h$  in depth forms on the surface. The grain boundary energy,  $\gamma_{GB}$ , should also be taken into account for the heterogeneous nucleation. Thus, when AB is added in the solution, the smaller critical size and lower formation energy barrier are able to offer increased nucleation rate.<sup>31–35</sup> Therefore, more nuclei are available for crystal growth, leading to the uniform nanosheet morphology. In addition, the high aspect ratio for the nanosheet is achieved, resulting from the strong anisotropic feature of nucleation.<sup>35</sup> In contrast, in the absence of AB, the formation energy barrier is increased, resulting in fewer nuclei and, therefore, bigger size, as well as ununiformed morphology (Figure S1). Finally, porous structures of mCVO and bCVO are formed due to the release of the crystallization water.<sup>36–38</sup>

The crystal structure of the products is determined by XRD characterization in Figure 2A. The resultant mCVO and bCVO show similar patterns, and both patterns match well with the monoclinic phase (JCPDS No. 01-77-1174, space group C2,  $a = 9.256 \text{ \AA}$ ,  $b = 3.508 \text{ \AA}$ ,  $c = 6.626 \text{ \AA}$ ,  $\alpha = \gamma = 90^\circ$ ,  $\beta = 111.55^\circ$ ). No peaks of impurities are detected. The mCVO retains its nanosheet morphology after annealing with no obvious structural collapse while the surface becomes rather rough (Figure 2B). The energy dispersive spectrometer (EDS) mapping analysis confirms that the elements Co, V, and O are homogeneously distributed in the macroporous structure (Figure S2). With the enlarged SEM image in Figure 2C, the macropores well-distributed on the nanosheets can be easily observed. The representative TEM image in Figure 2D shows the typical macroporous structure with the pore size of about 50 nm. The HRTEM image (Figure 2E) taken from the edge of nanosheet clearly shows visible lattice fringes with spacings of 3.0 and 2.7 Å, corresponding to the lattice plane of (201) and (110), respectively. The single crystalline nature of the particles is further confirmed by the SAED pattern in Figure 2F. However, for the bCVO, the SEM images in Figure S3A,B show that bCVO consists of big particles with rough surfaces. TEM images in Figure S3C,D reveal that the rough surface consists of randomly attached small particles. Furthermore, we choose the (110) diffraction peak to calculate the crystallite size of mCVO and bCVO. The average crystallite size of mCVO and bCVO can be calculated by using the Scherrer equation:

$$L = \frac{0.9\lambda_{k\alpha 1}}{B_{2\theta} \cos \theta_{\max}}$$

In this equation,  $L$  is the mean particle size, and  $\lambda_{k\alpha 1}$  is the X-ray wavelength ( $\lambda = 1.5418 \text{ \AA}$ ).  $\theta_{\max}$  is the peak position of (110) diffraction, and  $B_{2\theta}$  is the bandwidth at half height of the CVO (110) diffraction. After calculation, the particle size of mCVO is determined to be 138 nm, while that of bCVO is

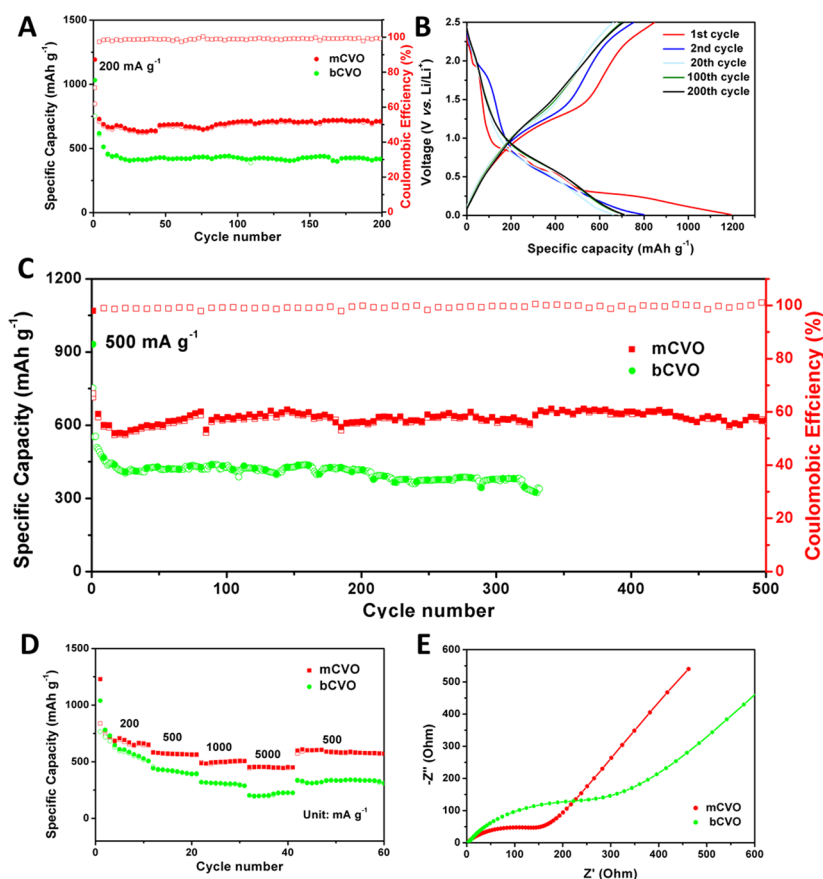


**Figure 4.** (A) Cycling performance of mCVO and bCVO at  $200 \text{ mA g}^{-1}$ . (B) Charge and discharge curves of mCVO at different cycles. (C) Long-life cycling performance of mCVO and bCVO at  $500 \text{ mA g}^{-1}$ . (D) Rate performance of mCVO and bCVO at current ranging from 200 to  $5000 \text{ mA g}^{-1}$ . (E) Alternating current–impedance plots of mCVO and bCVO.

calculated to be 208 nm, both of which are in good accordance with the TEM results. All these results indicate that utilizing AB to induce heterogeneous nucleation of cobalt vanadate leads to uniform macroporous nanosheet structure.

In order to investigate the transformation of the AB-assisted annealing process, the thermogravimetric-differential scanning calorimetry (TG-DSC) analysis of both mCVO and bCVO precursors is carried out in Figure 3A,B, respectively. For the bCVO precursor, the weight loss is divided into two parts, 100–400 and 400–600 °C, contributing to a total loss of 13.7% in Figure 3A. The weight loss suggests that the number of crystallization water in the precursor was near 2.3, which confirmed that our as-synthesized precursor was  $\text{CoV}_2\text{O}_6 \cdot 2.3\text{H}_2\text{O}$ . For mCVO precursor, three obvious weight losses are observed in the ranges 100–400, 400–470, and 470–600 °C, respectively, contributing to a total loss of 21.9% in Figure 3B. The corresponding DSC curve shows three broad peaks at 332, 422, and 491 °C, which are in good accordance with the TG curves. The initial two weight losses are very similar to that of the bCVO precursor, contributing a total loss of 15.8%. The weight loss between 100 and 470 °C is a bit higher while the two exothermic temperatures all shift slightly toward lower temperature when compared with that of the bCVO precursor. This may result from that in this process, as partial combustion of AB leads to greater weight loss, and the derived heat release decreases the reaction temperature needed for the release of crystallization water. The last weight loss of 6.1% at higher temperature of 491 °C results from the combustion of AB which is absent in bCVO precursor. The value accompanied by

the extra weight loss between 100 and 470 °C is consistent with the theoretical value (8.2%) of the AB content in the precursor, indicating the combustion of most of AB in the process. After annealing in air at 450 °C for 10 h, it is found that no obvious weight loss is observed up to 800 °C for mCVO, indicating that all AB is totally reacted (Figure S4). To further identify the origin of macropore formation, SEM images of products annealed at different temperatures are carried out. When the temperature is increased to 350 °C, the nanosheet morphology remains, and small pores start to appear; at 400 °C, the pores get larger, and at 450 °C, macroporous  $\text{CoV}_2\text{O}_6$  nanosheets are obtained. The further increase in temperature to 500 °C leads to the collapse of the two-dimensional morphology. On the basis of TG results, the combustion of AB occurs at over 450 °C while the removal of crystallization water occurs at 300–450 °C. Thus, it is safe to conclude that the formation of macropores is attributed to the removal of crystallization water.

In addition, the  $\text{N}_2$  adsorption/desorption measurements at 77 K were further examined to characterize the pore structure of the products (Figure 3C,D). The mCVO shows a surface area of  $13.5 \text{ m}^2 \text{ g}^{-1}$ , while the bCVO shows a relatively lower surface area of  $6.7 \text{ m}^2 \text{ g}^{-1}$ . Both samples show similar pore size distribution ranging around 50 nm on the basis of the Barrett–Joyner–Halenda (BJH) method which is consistent with the observation in the TEM. The higher surface area of mCVO results from the ordered nanosheet morphology and porous nanostructure, which may facilitate the ion diffusion and provide better electrochemical performance for lithium-ion batteries.

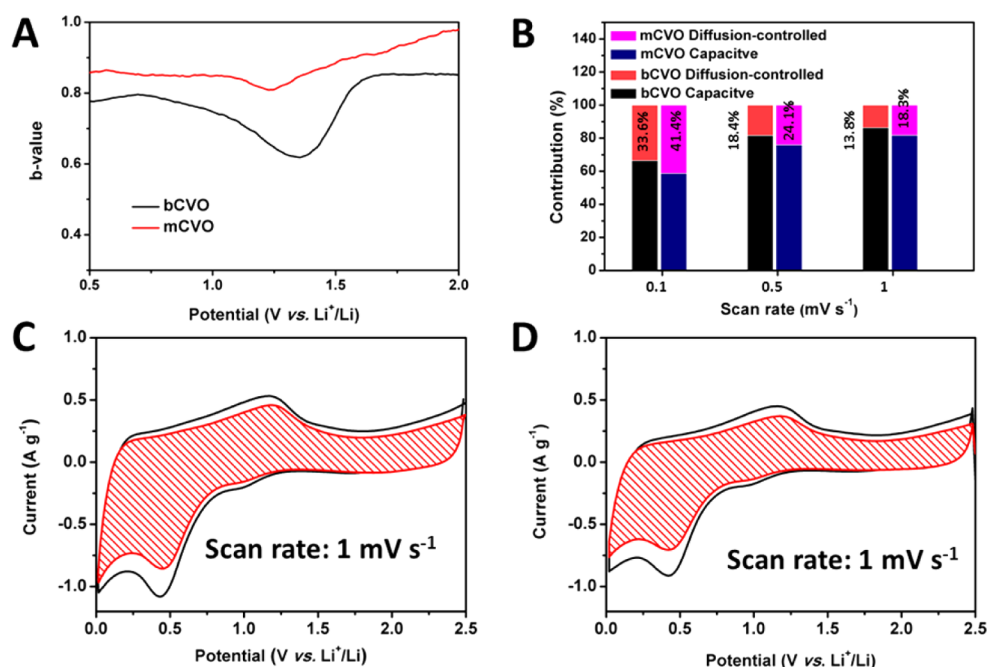


**Figure 5.** (A) Determination of the anodic  $b$ -values at different potential during charging. (B) Capacitive and diffusion-controlled contributions to charge storage in mCVO and bCVO at different scan rates of 0.1, 0.5, and 1  $\text{mV s}^{-1}$ . (C, D) Capacitive contributions of mCVO and bCVO to charge storage at 1  $\text{mV s}^{-1}$  at voltage range from 0.01 to 2.5 V, respectively. The shaded region is the contribution of the pseudocapacitive property.

The electrochemical performance of mCVO and bCVO is investigated. Initially, the CV curves of mCVO and bCVO are shown in Figure S6. Both samples exhibit the similar CV curves, implying their identical electrochemical behaviors. During the first cathodic sweep, two peaks are observed at around 0.57 and 0.17 V. The intense peak at 0.57 V is attributed to the disorganization of  $\text{CoV}_2\text{O}_6$  crystal structures, the formation of CoO and  $\text{Li}_x\text{V}_2\text{O}_5$ , and the formation of the SEI film on the fresh surface. Another intense reduction peak located at 0.17 V could be assigned to the further reduction of CoO in the  $\text{Li}_x\text{V}_2\text{O}_5$  matrix, which is similar to the reported literature.<sup>25,28,39</sup> The CV curves for the following cycles overlapped quite well indicating the excellent reversibility of the electrochemical reaction with few side reactions. The larger area of the CV curve of mCVO suggests the higher capacity achieved by mCVO. The cycling performance at 200  $\text{mA g}^{-1}$  in the voltage window of 0.01–2.5 V for up to 200 cycles and the corresponding charge–discharge curves at different cycles are shown in Figure 4A,B, respectively. During the initial cycle, the discharge and charge capacities are 1192 and 848  $\text{mAh g}^{-1}$ , which are equivalent to the insertion/extraction of approximately 14.7 and 10.4 Li per formula, and the coulombic efficiency is 71%. After the initial cycle, the following cycles show similar values in both the charge and discharge profiles indicating the high coulombic efficiency over 98.5%, further confirming the high reversibility of the electrochemical reaction. The mCVO shows excellent cycling stability with a capacity of 702  $\text{mAh g}^{-1}$  after 200 cycles, corresponding to the capacity retention of 88% against the second capacity. In comparison, bCVO shows rather poorer cycling performance with only 58% capacity left after 200 cycles (Figure S7). Furthermore, the long-time cyclability is evaluated at current density of 500  $\text{mA g}^{-1}$  in Figure 4C. The initial discharge and charge capacities of the mCVO are 1067 and 699  $\text{mAh g}^{-1}$ , respectively. Despite the initial capacity loss, the mCVO shows outstanding cyclability from the second cycle onward. The reversible

capacity at the the 500th cycle was 623  $\text{mA h g}^{-1}$  corresponding to the capacity retention of 89% against the second cycle. In comparison, the bCVO shows quick capacity decay after only 300 cycles, with merely 61% of the second capacity left. Besides the high capacity and stable cycle life, the rate performance is evaluated at different current densities ranging from 200 to 5000  $\text{mA g}^{-1}$  in Figure 4D. The capacity of 453  $\text{mAh g}^{-1}$  at 5000  $\text{mA g}^{-1}$  is retained, corresponding to 68% of that at 200  $\text{mA g}^{-1}$ . After the current density is recovered to 500  $\text{mA g}^{-1}$ , the capacity remains 581  $\text{mAh g}^{-1}$ , suggesting that no capacity decay is observed even after high current density. The capacity of mCVO is much lower than that of bCVO at each current indicating the better rate capability. Furthermore, the electrochemical impedance spectra (EIS) of the mCVO and bCVO show a compressed semicircle from the high- to medium-frequency range of each spectrum, and a line inclined at approximately 45° in the low-frequency range (Figure 4E). The compressed semicircle (Figure S8) describes the charge transfer resistance ( $R_{ct}$ ) for these electrodes, and the inclined line is considered as Warburg impedance ( $Z_w$ ). In the equivalent circuit,  $R_s$  represents the Ohmic resistance of the electrode system, including the electrolyte and the cell components.  $R_{ct}$  represents the resistance related to charge transfer, while CPE and  $Z_w$  are the capacitance related to double layer, and Warburg impedance, respectively. The  $R_s$  values of mCVO and bCVO are almost the same (Table S1), while the  $R_{ct}$  value of mCVO (44  $\Omega$ ) is higher than that of bCVO (134  $\Omega$ ), suggesting a reduced charge transfer resistance when compared to bCVO.

To examine the possible reasons for the improved rate capability and cycling stability, electrochemical kinetics was investigated.<sup>13,14</sup> The CV curves after the first cycle all exhibit broad cathodic and anodic peaks in different scan rates. Noticeably, both the cathodic and anodic peaks shift merely with scan rate increasing especially for mCVO (Figure S9), which is similar to the feature of pseudocapacitive material. Thus, a related analysis can be performed regarding the

behavior of the peak current by assuming the current,  $i$ , obeys a power law relationship with the sweep rate ( $i = a\nu^b$ ). Here,  $a$  is a constant, and  $\nu$  is the sweep rate. The  $b$ -value in the above equation is therefore an estimate of the type of charge storage occurring in the material: if  $b$  is 0.5, then the current is diffusion-controlled; if  $b$  is 1, the current is capacitive. The  $b$ -value analysis was performed using the CV data between 0.5 and 2.0 V in Figure 5A. For both mCVO and bCVO, the  $b$ -value is decreased to 0.5 especially in the range of redox peaks, indicating that the reaction that occurred in the peak range is rather diffusion-controlled while capacitive behavior dominates away from the peak range. A similar observation was reported on MoO<sub>2</sub> nanosheets,<sup>13</sup> and 10 nm TiS<sub>2</sub> nanosheet.<sup>14</sup> Furthermore, the  $b$ -value of mCVO is higher than that of bCVO at each potential, indicating that mCVO shows improved capacitive behavior over bCVO.

To be more precise, the diffusion and capacitive contributions are separated at a particular potential by using the equation below

$$i(V) = k_1\nu + k_2\nu^{1/2}$$

Solving  $k_1$  and  $k_2$  gives the capacitive and diffusion contributions to the current. Figure 5B shows the result of the analysis applied to mCVO and bCVO. For both mCVO and bCVO, the capacitive contribution increases with the scan rate. The best capacitive materials have minimal diffusion-controlled contributions, even at slow sweep rates, and this is what we observe in mCVO here. At a slow rate of 0.1 mV s<sup>-1</sup>, 33% capacity comes from the contribution of diffusion, while at 1 mV s<sup>-1</sup>, merely 13.8% is retained. Moreover, the capacitive contribution in mCVO is higher than that in bCVO at each scan rate. Typically, 86.2% and 81.7% of the total current are capacitive at 1 mV s<sup>-1</sup> for mCVO and bCVO, respectively. This clearly implies that mCVO offers more useful surface sites than bCVO, due to the macroporous structure, resulting in enhanced capacity and rate performance. In this analysis, it is generally most insightful to determine the different contributions at 1 mV s<sup>-1</sup> as this enables one to maximize the diffusive contribution to charge storage.<sup>14</sup> Thus, the capacity contributions of mCVO and bCVO at each potential are shown in Figure 5C,D, respectively. The pseudocapacitive contribution (shaded region) is characterized by broad peaks characteristic of surface-confined charge storage. As we observe in both mCVO and bCVO, the diffusion-controlled currents are located predominantly in the peak regions of the CV, as redox peaks are expected to be diffusion-controlled. The remaining regions are almost entirely capacitive which is consistent with the observation in  $b$ -value. The kinetic analysis (Figure 5C,D) shows that a large fraction of the stored charge comes from a capacitive process. This behavior is likely the result of the stable macroporous structure where the electrolyte can readily access the entire surface. Thus, it is not surprising that the rate-controlling step is surface limited rather than solid-state diffusion.<sup>15,16,40–42</sup>

Both the calculated  $b$ -value and capacitive contribution clearly demonstrate the unique characteristic behavior as a result of pseudocapacitance, which is different from the charge storage mechanism in classical batteries. It can be concluded that charge storage in CVO nanosheets follows a pseudocapacitive mechanism. This extrinsic behavior of the macroporous nanostructure is promoted by the fast Faradaic charge transfer kinetics at the interface and contribute to the enhanced kinetics that could be obtained due to the relative absence of diffusion.

In addition, the macroporous structure offers the large free space for volume expansion accommodation, with continuous current pathways that can facilitate electron transport and shorten lithium diffusion length.

## CONCLUSION

In summary, we have developed a facile AB induced heterogeneous growth of a macroporous CoV<sub>2</sub>O<sub>6</sub> nanosheet. Through kinetic analysis, the mCVO shows the following typical features of pseudocapacitive behavior: (1) currents that are mostly linearly dependent on sweep rate and (2) redox peaks whose potentials do not shift significantly with sweep rate. All these indicate that the mCVO shows an enhanced contribution of capacitive charge and displays the typical pseudocapacitive behavior. The macroporous CoV<sub>2</sub>O<sub>6</sub> nanosheets deliver a high reversible capacity of 702 mAh g<sup>-1</sup> at current density of 200 mA g<sup>-1</sup>, excellent cyclability with a capacity retention of 89% after 500 cycles at 500 mA g<sup>-1</sup>, and high rate capability of 453 mAh g<sup>-1</sup> at 5000 mA g<sup>-1</sup>. All these results demonstrate that the stable macroporous structure overcomes the limitation of the high-power capability of the bulk material. Our work provides a new direction for designing materials for energy storage devices with high rate capabilities.

## ASSOCIATED CONTENT

### Supporting Information

The Supporting Information is available free of charge on the ACS Publications website at DOI: 10.1021/acsami.6b00596.

SEM images of mCVO precursor and bCVO precursor, EDS mapping of mCVO, SEM images and TEM images of bCVO, TG curve of mCVO, CV curves of mCVO in the initial three cycles, cycle performance of mCVO at 500 mA g<sup>-1</sup>, and CV curves of mCVO and bCVO at different scan rate ranging from 0.1 to 1 mV s<sup>-1</sup> (PDF)

## AUTHOR INFORMATION

### Corresponding Authors

\*E-mail: liangzhou@whut.edu.cn.

\*E-mail: mlq518@whut.edu.cn.

### Author Contributions

L.Z., K.Z., and Y.L. contributed equally. The manuscript was written through contributions of all authors. All authors have given approval to the final version of the manuscript.

### Notes

The authors declare no competing financial interest.

## ACKNOWLEDGMENTS

This work was supported by the National Basic Research Program of China (2013CB934103, 2012CB933003), the International Science & Technology Cooperation Program of China (2013DFA50840), the National Natural Science Foundation of China (51302203, 51272197, 51521001), the National Science Fund for Distinguished Young Scholars (51425204), the Hubei Science Fund for Distinguished Young Scholars (2014CFA035), and the Fundamental Research Funds for the Central Universities (WUT: 2015-III-021, 2015-III-032, 2015-III-052, 2015-PY-2). We are deeply thankful to Professor Dongyuan Zhao of Fudan University, and Dr. Jun Liu of Pacific Northwest National Laboratory for their stimulating discussion and kind help.

## REFERENCES

- (1) Mai, L.; Tian, X.; Xu, X.; Chang, L.; Xu, L. Nanowire Electrodes for Electrochemical Energy Storage Devices. *Chem. Rev.* **2014**, *114* (23), 11828–11862.
- (2) Chu, S.; Majumdar, A. Opportunities and challenges for a sustainable energy future. *Nature* **2012**, *488* (7411), 294–303.
- (3) Larcher, D.; Tarascon, J.-M. Towards Greener and More Sustainable Batteries for Electrical Energy Storage. *Nat. Chem.* **2015**, *7*, 11.
- (4) Xu, W.; Xie, Z.; Cui, X.; Zhao, K.; Zhang, L.; Mai, L.; Wang, Y. Direct Growth of an Economic Green Energy Storage Material: a Monocrystalline Jarosite-KFe<sub>3</sub>(SO<sub>4</sub>)<sub>2</sub>(OH)<sub>6</sub>-nanoplates@rGO Hybrid as a Superior Lithium-ion Battery Cathode. *J. Mater. Chem. A* **2016**, *4*, 3735.
- (5) Zhao, K.; Zhang, L.; Xia, R.; Dong, Y.; Xu, W.; Niu, C.; He, L.; Yan, M.; Qu, L.; Mai, L. SnO<sub>2</sub> Quantum Dots@Graphene Oxide as a High-Rate and Long-Life Anode Material for Lithium-Ion Batteries. *Small* **2016**, *12*, 588–594.
- (6) Dong, Y. F.; Li, S.; Zhao, K. N.; Han, C. H.; Chen, W.; Wang, B. L.; Wang, L.; Xu, B.; Wei, Q. L.; Zhang, L.; Xu, X.; Mai, L. Q. Hierarchical Zigzag Na<sub>1.25</sub>V<sub>3</sub>O<sub>8</sub> Nanowires with Topotactically Encoded Superior Performance for Sodium-ion Battery Cathodes. *Energy Environ. Sci.* **2015**, *8* (4), 1267.
- (7) Zhang, L.; Zhao, K.; Xu, W.; Dong, Y.; Xia, R. L.; Fengning, H. L.; Wei, Q.; Yan, M.; Mai, L. Integrated SnO<sub>2</sub> Nanorod Array with Polypyrrole Coverage for High-rate and Long-life Lithium Batteries. *Phys. Chem. Chem. Phys.* **2015**, *17*, 7619.
- (8) Xu, W.; Zhao, K.; Niu, C.; Zhang, L.; Cai, Z.; Han, C.; He, L.; Shen, T.; Yan, M.; Qu, L.; Mai, L. Heterogeneous Branched Core-shell SnO<sub>2</sub>-PANI Nanorod Arrays with Mechanical Integrity and Three Dimensional Electron Transport for Lithium Batteries. *Nano Energy* **2014**, *8*, 196–204.
- (9) Magasinski, A.; Dixon, P.; Hertzberg, B.; Kvit, A.; Ayala, J.; Yushin, G. High-performance Lithium-ion Anodes Using a Hierarchical Bottom-up Approach. *Nat. Mater.* **2010**, *9*, 353.
- (10) Armstrong, A. R.; Lyness, C.; Panchmatia, P. M.; Islam, M. S.; Bruce, P. G. The Lithium Intercalation Process in the Low-voltage Lithium Battery Anode Li<sub>1+x</sub>V<sub>1-x</sub>O<sub>2</sub>. *Nat. Mater.* **2011**, *10*, 223.
- (11) Xin, S.; Guo, Y.-G.; Wan, L.-J. Nanocarbon Networks for Advanced Rechargeable Lithium Batteries. *Acc. Chem. Res.* **2012**, *45* (10), 1759.
- (12) Wang, C.; Wu, H.; Chen, Z.; McDowell, M. T.; Cui, Y.; Bao, Z. Self-healing Chemistry Enables the Stable Operation of Silicon Microparticle Anodes for High-energy Lithium-ion Batteries. *Nat. Chem.* **2013**, *5*, 1042.
- (13) Kim, H.; Cook, J. B.; Tolbert, S. H.; Dunn, B. The Development of Pseudocapacitive Properties in Nanosized-MoO<sub>2</sub>. *J. Electrochem. Soc.* **2015**, *162* (5), A5083–A5090.
- (14) Muller, G. A.; Cook, J. B.; Kim, H.; Tolbert, S. H.; Dunn, B. High Performance Pseudocapacitor Based on 2D Layered Metal Chalcogenide Nanocrystals. *Nano Lett.* **2015**, *15* (3), 1911–1917.
- (15) Zhu, Y.; Peng, L.; Chen, D.; Yu, G. Intercalation Pseudocapacitance in Ultrathin VOPO<sub>4</sub> Nanosheets: Toward High-Rate Alkali-Ion-Based Electrochemical Energy Storage. *Nano Lett.* **2016**, *16*, 742.
- (16) Li, S.; Qiu, J.; Lai, C.; Ling, M.; Zhao, H.; Zhang, S. Surface Capacitive Contributions: Towards High Rate Anode Materials for Sodium ion Batteries. *Nano Energy* **2015**, *12*, 224–230.
- (17) Li, C.; Han, X.; Cheng, F.; Hu, Y.; Chen, C.; Chen, J. Phase and Composition Controllable Synthesis of Cobalt Manganese Spinel Nanoparticles towards Efficient Oxygen Electrocatalysis. *Nat. Commun.* **2015**, *6*, 7345.
- (18) Zhang, G.; Lou, X. D. General Synthesis of Multi-Shelled Mixed Metal Oxide Hollow Spheres with Superior Lithium Storage Properties. *Angew. Chem., Int. Ed.* **2014**, *53* (34), 9041–9044.
- (19) Yuan, C.; Wu, H. B.; Xie, Y.; Lou, X. D. Mixed Transition-Metal Oxides: Design, Synthesis, and Energy-Related Applications. *Angew. Chem., Int. Ed.* **2014**, *53* (6), 1488–1504.
- (20) Denis, S.; Baudrin, E.; Orsini, F.; Ouvrard, G.; Touboul, M.; Tarascon, J.-M. Synthesis and Electrochemical Properties of Numerous Classes of Vanadates. *J. Power Sources* **1999**, *81–82*, 79–84.
- (21) Yang, G.; Song, H.; Yang, G.; Wu, M.; Wang, C. 3D hierarchical AlV<sub>3</sub>O<sub>9</sub> microspheres: First synthesis, excellent lithium ion cathode properties, and investigation of electrochemical mechanism. *Nano Energy* **2015**, *15*, 281–292.
- (22) An, Q.; Lv, F.; Liu, Q.; Han, C.; Zhao, K.; Sheng, J.; Wei, Q.; Yan, M.; Mai, L. Amorphous Vanadium Oxide Matrixes Supporting Hierarchical Porous Fe<sub>3</sub>O<sub>4</sub>/Graphene Nanowires as a High-Rate Lithium Storage Anode. *Nano Lett.* **2014**, *14* (11), 6250–6256.
- (23) Sim, D. H.; Rui, X.; Chen, J.; Tan, H.; Lim, T. M.; Yazami, R.; Hng, H.; Yan, Q. Direct Growth of FeVO<sub>4</sub> Nanosheet Arrays on Stainless Steel Foil as High-performance Binder-free Li ion Battery Anode. *RSC Adv.* **2012**, *2*, 3630.
- (24) Wu, F.; Xiong, S.; Qian, Y.; Yu, S. Hydrothermal Synthesis of Unique Hollow Hexagonal Prismatic Pencils of Co<sub>3</sub>V<sub>2</sub>O<sub>8</sub> · n H<sub>2</sub>O: A New Anode Material for Lithium-Ion Batteries. *Angew. Chem., Int. Ed.* **2015**, *54* (37), 10787–10791.
- (25) Wu, F.; Yu, C.; Liu, W.; Wang, T.; Feng, J.; Xiong, S. Large-scale synthesis of Co<sub>2</sub>V<sub>2</sub>O<sub>7</sub> hexagonal microplatelets under ambient conditions for highly reversible lithium storage. *J. Mater. Chem. A* **2015**, *3*, 16728.
- (26) Yin, Z.; Xiao, Y.; Wang, X.; Wang, W.; Zhao, D.; Cao, M. MoV<sub>2</sub>O<sub>8</sub> nanostructures: controlled synthesis and lithium storage mechanism. *Nanoscale* **2016**, *8* (1), 508–516.
- (27) Wu, F.; Bai, J.; Feng, J.; Xiong, S. Porous Mixed Metal Oxides: Design, Formation Mechanism, and Application in Lithium-ion Batteries. *Nanoscale* **2015**, *7* (41), 17211–17230.
- (28) Yang, G.; Cui, H.; Yang, G.; Wang, C. Self-Assembly of Co<sub>3</sub>V<sub>2</sub>O<sub>8</sub> Multilayered Nanosheets: Controllable Synthesis, Excellent Li-Storage Properties, and Investigation of Electrochemical Mechanism. *ACS Nano* **2014**, *8*, 4474–4487.
- (29) Gan, L.; Deng, D.; Zhang, Y.; Li, G.; Wang, X.; Jiang, L.; Wang, C. Zn<sub>3</sub>V<sub>2</sub>O<sub>8</sub> Hexagon Nanosheets: a High-performance Anode Material for Lithium-ion Batteries. *J. Mater. Chem. A* **2014**, *2* (8), 2461.
- (30) Narayanan, R.; Bandaru, P. R. High Rate Capacity through Redox Electrolytes Confined in Macroporous Electrodes. *J. Electrochem. Soc.* **2015**, *162* (1), A86–A91.
- (31) Chung, S.; Kim, Y.; Choi, S.; Kim, J.-G. Capturing Heterogeneous Nucleation of Nanoscale Pits and Subsequent Crystal Shrinkage during Ostwald Ripening of a Metal Phosphate. *ACS Nano* **2015**, *9*, 327.
- (32) Kwon, S. G.; Krylova, G.; Phillips, P. J.; Klie, R. F.; Chattopadhyay, S.; Shibata, T.; Bunel, E. E.; Liu, Y.; Prakapenka, V. B.; Lee, B.; Shevchenko, E. V. Heterogeneous Nucleation and Shape Transformation of Multicomponent Metallic Nanostructures. *Nat. Mater.* **2014**, *14*, 215–223.
- (33) Pouget, E. M.; Bomans, P. H. H.; Goos, J. A. C. M.; Frederik, P. M.; de With, G.; Sommerdijk, N. A. J. M. The Initial Stages of Template-Controlled CaCO<sub>3</sub> Formation Revealed by Cryo-TEM. *Science* **2009**, *323*, 1455.
- (34) Gebauer, D.; Völkel, A.; Cölfen, H. Stable Prenucleation Calcium Carbonate Clusters. *Science* **2008**, *322*, 1819–1822.
- (35) Yin, X.; Shi, J.; Niu, X.; Huang, H.; Wang, X. Wedding Cake Growth Mechanism in One-Dimensional and Two-Dimensional Nanostructure Evolution. *Nano Lett.* **2015**, *15*, 7766–7772.
- (36) Su, X.; Fu, F.; Yan, Y.; Zheng, G.; Liang, T.; Zhang, Q.; Cheng, X.; Yang, D.; Chi, H.; Tang, X.; Zhang, Q.; Uher, C. Self-propagating High-temperature Synthesis for Compound Thermoelectrics and New Criterion for Combustion Processing. *Nat. Commun.* **2014**, *5*, 4908.
- (37) An, Q.; Zhang, P.; Xiong, F.; Wei, Q.; Sheng, J.; Wang, Q.; Mai, L. Three-dimensional Porous V<sub>2</sub>O<sub>5</sub> Hierarchical Octahedrons with Adjustable Pore Architectures for Long-life Lithium Batteries. *Nano Res.* **2015**, *8* (2), 481–490.
- (38) An, Q.; Zhang, P.; Wei, Q.; He, L.; Xiong, F.; Sheng, J.; Wang, Q.; Mai, L. Top-down Fabrication of Three-dimensional Porous V<sub>2</sub>O<sub>5</sub> Hierarchical Microplates with Tunable Porosity for Improved Lithium Battery Performance. *J. Mater. Chem. A* **2014**, *2* (10), 3297.

(39) Luo, Y.; Xu, X.; Zhang, Y.; Chen, C.; Zhou, L.; Yan, M.; Wei, Q.; Tian, X.; Mai, L. Graphene Oxide Templated Growth and Superior Lithium Storage Performance of Novel Hierarchical  $\text{Co}_2\text{V}_2\text{O}_7$  Nanosheets. *ACS Appl. Mater. Interfaces* **2016**, *8*, 2812.

(40) Lim, E.; Jo, C.; Kim, H.; Kim, M.; Mun, Y.; Chun, J.; Ye, Y.; Hwang, J.; Ha, K.; Roh, K.; Kang, K.; Yoon, S.; Lee, J. Facile Synthesis of  $\text{Nb}_2\text{O}_5$ @Carbon Core@Shell Nanocrystals with Controlled Crystalline Structure for High-Power Anodes in Hybrid Supercapacitors. *ACS Nano* **2015**, *9*, 7497–7505.

(41) Lübke, M.; Marchand, P.; Brett, J. L.; Shearing, P.; Gruar, R.; Liu, Z.; Darr, J. A. High Power Layered Titanate Nano-sheets as Pseudocapacitive Lithium-ion Battery Anodes. *J. Power Sources* **2016**, *305*, 115–121.

(42) Zhao, K.; Liu, F.; Niu, C.; Xu, W.; Dong, Y.; Zhang, L.; Xie, S.; Yan, M.; Wei, Q.; Zhao, D.; Mai, L. Graphene Oxide Wrapped Amorphous Copper Vanadium Oxide with Enhanced Capacitive Behavior for High-Rate and Long-Life Lithium-Ion Battery Anodes. *Adv. Sci.* **2015**, *2* (12), 201500154.